Engineering Journal

issn: 0125-8281

Article

Compressive Behaviors of Micropillar Sheets Made of PDMS Material Using the Finite Element Method

Thitikan Pakawan[1,a], Tumrong Puttapitukporn[1,b,*], Nithi Atthi[2,c], Witsaroot Sripumkhai[2], Pattaraluck Pattamang[2], Nipapan Klunngien[2], and Wutthinan Jeamsaksiri[2]

1 Department of Mechanical Engineering, Faculty of Engineering, Kasetsart University, Bangkok 10900, Thailand
2 Thai Microelectronics Center (TMEC), National Electronics and Computer Technology Center (NECTEC), Chachoengsao 24000, Thailand
E-mail: [a]thitikan.work@gmail.com, [b]fengtop@ku.ac.th (Corresponding author), [c]nithi.atthi@nectec.or.th

Abstract. Thai Microelectronics Center fabricates micropillar sheets from soft lithography techniques and roll-to-roll process which were used as superhydrophobic and superoleophobic surfaces coated on marine structures and medical devices. This research aimed to study appropriate constitutive models and mechanical behaviours of PDMS micropillar sheets with two substrate thicknesses of 1,910 µm and 150 µm under compressive loading using ANSYS Mechanical APDL program. The constitutive models consisted of Mooney-Rivlin (2, 3 and 5 parameters), Ogden (1st, 2nd and 3rd orders), Neo-Hookean, Polynomial (1st and 2nd orders), Arruda-Boyce, Gent and Yeoh (1st, 2nd and 3rd orders) models were curved fitting with experiment data from uniaxial compression test. We found that the most accurate constitutive model was Mooney-Rivlin 5 parameter model for the low strain range $(\varepsilon_{\tilde{z}} \leq 0.225)$. The compressive strength and the lateral collapse of micropillars depended on substrate thickness were studied. The lateral collapse of micropillars was found when the substrate thicknesses were 150 µm and 1,910 µm. As the substrate thickness decreased, the compressive strength decreased while the elastic stiffness increased. The maximum compressive forces per one micropillar were 21.060 µN and 18.549 µN for the 1,910 µm and 150 µm thick substrates respectively.

Keywords: Finite element analysis, hyperelastic material model, hydrophobic, polydimethylsiloxane, micropillar sheet, compressive strength.

ENGINEERING JOURNAL Volume 24 Issue 4
Received 2 December 2019
Accepted 30 March 2020
Published 31 July 2020
Online at https://engj.org/
DOI:10.4186/ej.2020.24.4.73

DOI:10.4186/ej.2020.24.4.73

1. Introduction

Biofouling of virus, bacteria, and disease on medical equipment surface is a leading cause of human infection which can be a cause of death. Furthermore, biofouling of seaweed, bacteria, and barnacles in marine engineering structures is a major cause of structural damage and financial losses [1]. As result, many researches have focused on development of antifouling surfaces, especially superhydrophobic films coated on medical equipment and marine engineering structures. Polydimethylsiloxane (PDMS) materials are commonly used to fabricate superhydrophobic surfaces because of their low surface energy, good thermal and oxidative stability, non-toxic, and good biocompatibility [2]. The hydrophobic properties are classified by wetting contact angles. Gao and Yan [3] classified the wettability property of surfaces by a water contact angle. Firstly, if the water contact angle is smaller than 90 degrees, it is called a hydrophilic surface. Secondly, if the water contact angle is between 90 to 150 degrees, it is called a hydrophobic surface. Thirdly, if the water contact angle is greater than 150 degrees, it is called a superhydrophobic surface. This surface can prepare from hydrophobic surfaces by creating rough surface which made of micro- or nano-structures on substrate surfaces [4]. Many researches have studied on both micro- and nano-patterns which prevent biofouling and also mechanical behaviours of hydrophobic surfaces under external loads by using the finite element method. Atthi et al. [5] studied effects of various asperity shapes on water contact angles in superhydrophobic surfaces. The authors found that the pentagonal pillar shape has 1-7 degrees higher water contact angle than the other conventional pillar shapes, and produced a superhydrophobic surface with the highest water contact angle of 155.9 degrees. Graham and Cady [6] found that the sharklet pattern on hydrophobic surface could withstand biofouling. Cheng et al. [7] studied the mechanical properties of PDMS materials with various sizes and aspect ratio. The authors found that size and aspect ratio of micropillars effected on Young's modulus. Singh et al. [8] used the finite element method to study deformation of taper and tapered-free pillars subjected to compressive load. Their FE results showed that straight pillars had more compressive strength than tapered pillars. Thanakhun and Puttapitukporn [9] studied the most appropriate constitutive model to analyze structural behaviors of micropillars made of pure PDMS and PUA core coated PDMS subjected to shear loadings in ANSYS Mechanical APDL program. The Neo-Hookean, Mooney-Rivlin (3 and 5 parameters), Ogden (1st, 2nd, 3rd orders), Yeoh (1st, 2nd, 3rd orders) and Arruda-Boyce material models were used to curve fitting experimental data from uniaxial tensile test. The authors found that the most accurate model was the Yeoh 3rd order model for both uniaxial tensile and punch-shear loadings (for low strain region) and the PUA core coated with 100 nm-thick PDMS micropillar showed better lateral strength than pure PDMS micropillar. Johari and Shyan [10] analyzed effect of height and diameter of the cylindrical micropillar which made of PDMS material under shear forces in ANSYS program. The FE results showed that the deformation increases when micropillar height increased and micropillar diameter decreased. Rathod et al. [11] used the finite element method to study the most suitable material models for PDMS micropillar subjected to traction forces in ABAQUS program. The authors found that the Neo-Hookean model obtained more accurate results than Arruda-Boyce models. Kim, Kim and Jeong [12] studied constitutive models of PDMS specimens under uniaxial tensile test in MSC Marc program. The Neo-Hookean, Mooney-Rivlin 3 parameters and Ogden 2nd order material models were studied and the authors found that Ogden 2nd order model was the most accurate results under the large strain range. Carlescu, Prisacaru and Olaru [13] studied mechanical behaviour of soft elastomers based on PDMS under uniaxial tension test in ABAQUS/CAE program. The Mooney-Rivlin, Ogden, Neo-Hookean, Yeoh, Arruda-Boyce and Van der Waals material models were used to curve fitting experimental data from uniaxial tensile test. The authors found that Mooney-Rivlin, Ogden and Yeoh models were obtained the most accurate results. Phromjan and Suvanjumrat [14] studied suitable constitutive models of the solid tire subjected to compressive load in MSC Marc program. The Polynomial, Arruda-Boyce, Mooney-Rivlin, Yeoh and Ogden material models were used to curve fitting with experiment data from uniaxial compression test. The authors found that Ogden model obtained the most accurate results. Rugsaj and Suvanjumrat [15] used the finite element method to study appropriated material model for Non-Pneumatic tire subjected to tensile and compressive loads. Their FE results were compared with the experiment data. The authors found that the Mooney-Rivlin model obtained the most accurate FE results for tensile test while the Ogden model obtained the most accurate FE results for compressive test. Cheng et al. [16] studied strength of micropillar arrays with liquid crystal thin films between micropillars in Surface Evolver program. The authors found that liquid crystal in the micropillar arrays were robust and resistant to gravitational forces and mechanical shock. Huri and Mankovits [17] studied the most appropriate constitutive model for rubber materials subjected to compressive load in ANSYS program. Their constitutive models were Mooney-Rivlin and Yeoh models which were determined their accuracies with the sum of squared errors (SSE). The authors showed that the Yeoh model obtained the most accurate FE results. Wu et al. [18] used the explicit finite element method to analysis the sliding lead rubber bearing (SLRB) by using ANSYS/LS-DYNA program. The Mooney-Rivlin model was applied into FE modelling. Their FE results showed that the modelling method could reproduce the vertical stiffness and particular hysteresis behaviour of the bearing.

This research aimed to study appropriate constitutive models and mechanical behaviours of PDMS micropillar sheets with two substrate thicknesses of 1,910 μm to 150 μm under compressive loading using ANSYS Mechanical

APDL program. The constitutive models consisted of Mooney-Rivlin (2, 3 and 5 parameters), Ogden (1st, 2nd and 3rd orders), Neo-Hookean, Polynomial (1st and 2nd orders), Arruda-Boyce, Gent and Yeoh (1st, 2nd and 3rd orders) models were curved fitting with experiment data from uniaxial compression test.

2. Theory

2.1. Hyperelastic Material Models

The constitutive model of hyperelastic materials describes a nonlinear stress-strain relationship which expresses abilities of materials to experience large deformation under small loads and to recover their initial shape upon unloading [19]. In this research, the constitutive models of PDMS material were the Neo-Hookean, Mooney-Rivlin (2, 3 and 5 parameters), Polynomial (1st and 2nd orders), Yeoh (1st, 2nd and 3rd orders), Ogden (1st, 2nd and 3rd orders), Arruda-Boyce and Gent models. The typical strain energy density function (W) can be written in terms of the invariants ($\bar{I}$) and stretch ratios (λ). The invariants can be written as

$$\bar{I}_1 = \lambda_1^2 + \lambda_2^2 + \lambda_3^2 \quad (1)$$

$$\bar{I}_2 = \lambda_1^2\lambda_2^2 + \lambda_2^2\lambda_3^2 + \lambda_1^2\lambda_3^2 \quad (2)$$

$$\bar{I}_3 = \lambda_1^2\lambda_2^2\lambda_3^2 \quad (3)$$

The stretch ratio in the i-direction can be written as

$$\lambda_i = \frac{L_i}{(L_0)_i} = 1 + \varepsilon_i \quad (4)$$

where $(L_0)_i$, L_i and ε_i are the initial length, the instantaneous length and the engineering strain in the i-direction respectively. The principal stress (σ) in the i-direction is derived from the strain energy function as

$$\sigma_i = \lambda_i \frac{\partial W}{\partial \lambda_i} \quad (5)$$

2.1.1. Neo-Hookean model

The Neo-Hookean model is developed from Hooke's law. This constitutive model is simple to use and good agreement with experiment data in relatively small strains. The strain energy density function of Neo-Hookean model can be written as in Eq. (6).

$$W = \frac{\mu}{2}\left(\bar{I}_1 - 3\right) + \frac{1}{D}\left(J_{el} - 1\right)^2 \quad (6)$$

where $\bar{I}_1$ is the 1st invariant, μ is an initial shear modulus, D is a material incompressibility constant and J_{el} is elastic volumetric ratio.

2.1.2. Mooney-Rivlin model

The Mooney-Rivlin model is developed from Neo-Hookean model. The strain energy density function of Mooney-Rivlin model depends on the 1st and 2nd invariants and can be written as in Eq. (7).

$$W = \sum_i \sum_j C_{ij}\left(\bar{I}_1 - 3\right)^i \left(\bar{I}_2 - 3\right)^j + D\left(J_{el} - 1\right)^2 \quad (7)$$

where C_{ij} is material constants, $\bar{I}_2$ is the 2nd invariant.

2.1.3. Polynomial model

The strain energy density function of Polynomial model is formulated in terms of the 1st and 2nd invariants and can be written as in Eq. (8).

$$W = \sum_{i,j=0}^{N} C_{ij}\left(\bar{I}_1 - 3\right)^i \left(\bar{I}_2 - 3\right)^j + \sum_{i=1}^{N} \frac{1}{D_i}\left(J_{el} - 1\right)^{2i} \quad (8)$$

where D_i is the i^{th} material incompressibility constant and N is the number of polynomial terms.

2.1.4. Yeoh model

The strain energy density function of Yeoh model can be formulated from only the 1st invariants and is written as in Eq. (9).

$$W = \sum_{i=1}^{3} C_{i0}\left(\bar{I}_1 - 3\right)^i + \sum_{i=1}^{3} \frac{1}{D_i}\left(J_{el} - 1\right)^{2i} \quad (9)$$

where C_{io} is a material constant.

2.1.5. Ogden model

The Ogden model can be defined the strain energy density function (W) based on principle stretches ($\bar{\lambda}_i$) which is written by the following equation.

$$W = \sum_{i=1}^{N} \frac{2\mu_i}{\alpha_i^2}\left(\bar{\lambda}_1^{\alpha_i} + \bar{\lambda}_2^{\alpha_i} + \bar{\lambda}_3^{\alpha_i} - 3\right) + \sum_{i=1}^{N} \frac{1}{Di}\left(J_{el} - 1\right)^{2i} \quad (10)$$

where μ_i and α_i are material constants, N is the number of Ogden terms.

2.1.6. Arruda-Boyce model

The Arruda-Boyce model expressed the strain energy density function based on molecular chain network which is called 8-chain model. The strain energy density function is written as in Eq. (11).

DOI:10.4186/ej.2020.24.4.73

$$W=\mu\begin{pmatrix}\frac{1}{2}\left(\bar{I}_1-3\right)\\+\frac{1}{20\lambda_L^2}\left(\bar{I}_1^2-9\right)\\+\frac{11}{1050\lambda_L^4}\left(\bar{I}_1^3-27\right)\\+\frac{19}{7000\lambda_L^6}\left(\bar{I}_1^4-81\right)\\+\frac{519}{673750\lambda_L^8}\left(\bar{I}_1^5-243\right)\end{pmatrix}+\frac{1}{D}\left(\frac{J_{el}^2-1}{2}-\ln J_{el}\right) \quad (11)$$

where λ_L is the limiting network stretch.

2.1.7. Gent model

The Gent model is a simple and clear mathematical structure of the constitutive model [20]. This model formulated based on only 1st invariants as shown in Eq. (12).

$$W=-\frac{\mu}{2}J_m\ln\left(1-\frac{\bar{I}_1-3}{J_m}\right) \quad (12)$$

where J_m is the maximum value of 1st invariants.

2.2. Accuracy of Hyperelastic Material Models

The accuracies of FE models were determined by sum square of error (SSE) [21] as written in Eq. (13).

$$SSE=\sum_{i=1}^{n}\left(y_i-\hat{y}\right)^2 \quad (13)$$

where y_i is the stress obtained from the laboratory and $\hat{y}$ is the stress obtained from the finite element analysis.

3. Methodology

3.1. Uniaxial Compression Test

3.1.1. Laboratory experiment of uniaxial compression test

Compressive specimens were made of a PDMS material which has ratio of a PDMS monomer to a curing agent ratio of 10:1. The compression test was performed with a universal testing machine (Instron 55R4502) on five cylindrical specimens at room temperature of 24 ° C, the cross head speed of 5 mm/min and humidity of 53 % R.H as described in ASTM D575-91. Figure 1a illustrates test specimens which made of PDMS material and their dimension are shown in Table 1. To reduce the Mullins effect, each uniaxial compression test was performed repeatedly three times and the third time data was collected. The maximum vertical displacement of specimens was specified at -50% of their original thickness as shown in Fig. 1b. The stress-strain relationships of uniaxial compression test were shown in Fig. 2.

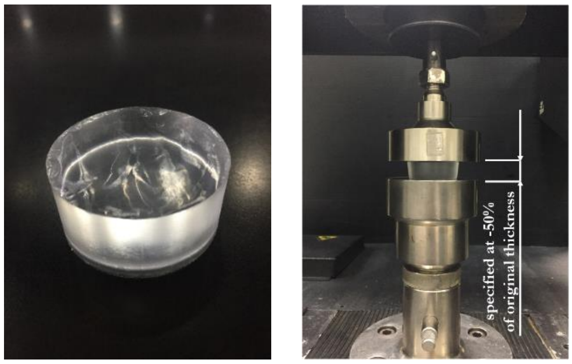

(a) (b)

Fig. 1. (a) A cylindrical specimen and (b) The specimen installed in a universal testing machine (Instron 55R4502).

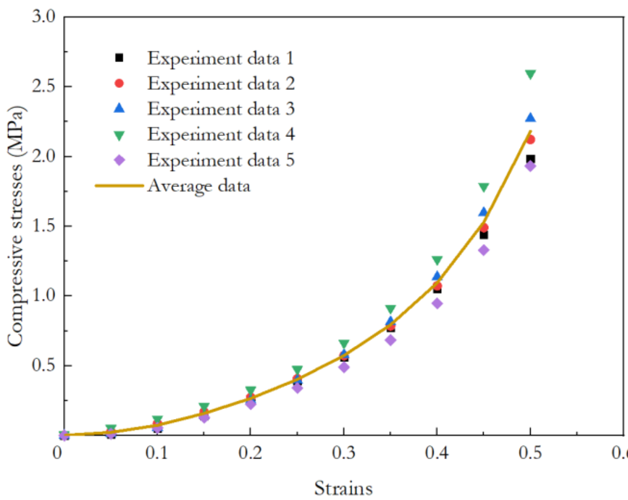

Fig. 2. Plot of engineering compressive stresses and strains of experiment data and an average data for uniaxial compression test.

Table 1. Dimension of cylindrical specimens.

Specimen number	Diameter (mm)	Thickness (mm)
1	38.54	16
2	38.13	16.52
3	38.36	16.53
4	38.22	16.89
5	38.88	16.1
Average	38.43	16.41
SD	0.30	0.36

3.1.2. Finite element analysis of uniaxial compression test

The finite element analysis was performed to determine accuracy of hyperelastic material models by using ANSYS Mechanical APDL program. The constitutive equations of Neo-Hookean, Mooney-Rivlin (2, 3 and 5 parameters), Polynomial (1st and 2nd orders), Yeoh (1st, 2nd and 3rd orders), Ogden (1st, 2nd and 3rd orders), Arruda-Boyce and Gent models were studied for their accuracies in ANSYS program. Tables 2-8 illustrate material constants of each hyperelastic material models obtained from the curve fitting of experimental data from compressive test in ANSYS program. The finite element model of the cylindrical specimen had a diameter of 38.43 mm and thickness of 16.41 mm as shown in Fig. 3. The FE models were meshed using SOLID186 elements which were 20-nodes structural solid elements and had 3 translations in the x, y, and z directions for each node. This FE model is consisted of 30,899 nodes with 6,912 elements. The boundary conditions were that the lower end was fixed in tangential direction and z-direction while the upper end was gradually applied the vertical displacement of 8.5 mm in the z-direction.

Table 2. The material constants of Polynomial model.

Material constants	Polynomial model	
	1st order	2nd order
C_{10}	-0.21162	-0.16808
C_{01}	0.28638	0.23398
C_{11}		-2.54487
C_{20}		2.09914
C_{02}		0.78043
D_1	0	0
D_2		0

Table 3. The material constants of Neo-Hookean model.

Material constants	Neo-Hookean model
μ	0.25012
D	0

Table 4. The material constants of Mooney-Rivlin model.

Material constants	Mooney-Rivlin model		
	2 parameters	3 parameters	5 parameters
C_{10}	-0.21162	-0.44501	-0.16808
C_{01}	0.28638	0.50429	0.23398
C_{11}		-0.0622	-2.54487
C_{20}			2.09914
C_{02}			0.78043
D	0	0	0

Table 5. The material constants of Arruda-Boyce model.

Material constants	Arruda-Boyce model
μ	1.93 x 10^{-8}
λ_L	0.12488
D	0

Table 6. The material constants of Yeoh model.

Material constants	Yeoh model		
	1st order	2nd order	3rd order
C_{10}	0.12506	0.09511	0.08454
C_{20}		0.11852	0.24102
C_{30}			-0.09507
D_1	0	0	0
D_2		0	0
D_3			0

Table 7. The material constants of Ogden model.

Material constants	Ogden model		
	1st order	2nd order	3rd order
μ_1	12397.0691	5.11284	4.36077
α_1	0.00004	0.04722	0.03681
μ_2		5.11285	4.36085
α_2		0.04713	0.03693
μ_3			4.36099
α_3			0.03688
D_1	0	0	0
D_2		0	0
D_3			0

Table 8. The material constants of Gent model.

Material constants	Gent model
μ	0.00222
J_m	0.99739

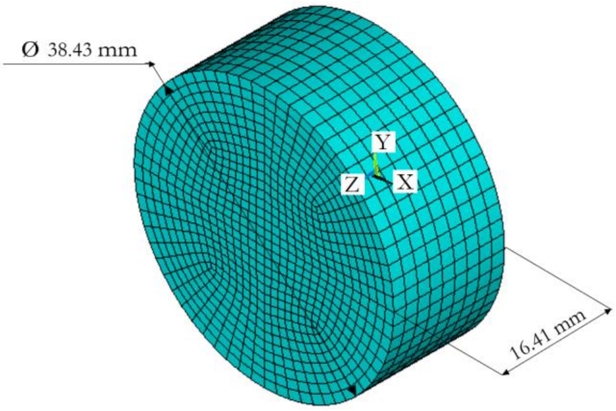

Fig. 3. FE model of uniaxial compression test.

3.2. Finite Element Analysis of Micropillar Sheets

A 2 cm x 3 cm x 0.2 cm micropillar sheet was fabricated from PDMS material (with a ratio of a PDMS monomer to a curing agent ratio of 10:1) by soft lithography techniques at Thai Microelectronics Center (TMEC) as shown in Fig. 4. With the new roll-to-roll fabrication technique, the substrate thickness of the micropillar sheet could be reduced from 1,910 μm to 150 μm. This research aimed to study effects of decreasing the substrate thickness of the micropillar sheet on its compressive strength.

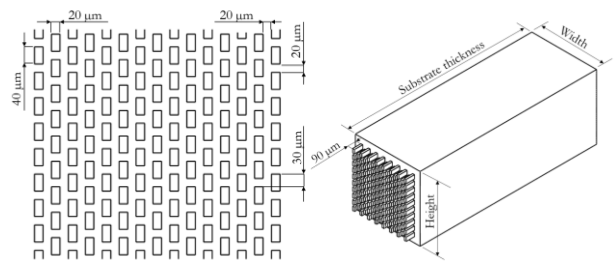

Fig. 4. Dimension of a micropillar sheet.

To reduce FE computational time, micropillars having dimension of 20 μm x 40 μm x 90 μm were created into array patterns on 150 and 1,910 μm thick substrates which composed of 1, 56, 70 and 84 micropillars respectively as shown in Fig. 5-6. The substrate height and substrate width were modeled long enough for studying only effects on interaction between micropillars as listed in Table 9. The FE models were meshed by using SOLID186 elements. The number of elements of each FE models are shown in Table 10. Their boundary conditions of FE models with substrates were that all nodes on the top surface of micropillar sheet were coupled vertical displacement in the z-direction while all nodes on bottom surface of the substrate were fixed in all degree of freedom. All contact areas between nearby micropillars were set as surface-to-surface frictionless contacts. To evaluate effects of a substrate thickness on compressive strength of a micropillar sheet, the FE model of a micropillar without a substrate was studied as shown in Fig. 7. This FE model consisted of 3,109 nodes with 576 elements. The boundary conditions were that all nodes on the top surface of a micropillar were coupled vertical displacement in the z-direction while all nodes on the bottom surface were fixed in all degree of freedom.

Table 9. FE model of a micropillar sheet with a substrate.

Number of micropillars	Width (μm) x height (μm)	
	150 μm thick substrate	1,910 μm thick substrate
1 micropillar	700 x 700	600 x 600
56 micropillars	1,300 x 1,300	2,000 x 2,000
70 micropillars	1,300 x 1,300	2,000 x 2,000
84 micropillars	1,300 x 1,300	2,400 x 2,000

Table 10. The number of elements of each FE models with the substrate thickness of 150 μm and 1,910 μm.

Number of micropillars	Number of elements	
	150 μm thick substrate	1,910 μm thick substrate
1 micropillar	4,972	3,672
56 micropillars	28,852	51,952
70 micropillars	31,948	55,048
84 micropillars	35,044	106,144

4. Results and Discussion

4.1. Finite Element Results of a Uniaxial Compression Test

The plot of true compressive stresses and strains of each hyperelastic material models as shown in Fig. 8. The accuracies of FE models were determined by sum square of error (SSE) which were illustrated in Table 11. Here, the Mooney-Rivlin 5 parameters model obtained the most accurate FE results (with SSE of 106.17×10^{-6}) for low strain range of $\varepsilon_z \leq 0.225$ as shown in Fig. 9. Figure 10 shows the contour plot of the stress and strain in z-direction of the FE model using Mooney-Rivlin 5 parameter model.

4.2. Finite Element Results of Micropillar Sheets

The compressive strength of micropillar sheets and interactions between micropillars were studied. The lateral collapse of micropillars were found and will result in loss of hydrophobic properties because of cohesive forces [22]. Figure 11 shows the plot of compressive force per one micropillar and vertical displacement for FE models which had 1, 56, 70 and 84 micropillars on the 1,910 μm thick substrate. We found convergence of the FE results for the FE model with 84 micropillars. Furthermore, the plot of compressive force per one micropillar and vertical displacement for FE models which had 1, 56, 70 and 84 micropillars on the 150 μm thick substrate as shown in Fig. 12. Again, we found convergence of the FE results

DOI:10.4186/ej.2020.24.4.73

for the FE model with 84 micropillars. The plot of compressive force and vertical displacement of 84 micropillars for various substrate thicknesses is shown in Fig 13. Figure 14 shows contour plot of deformation in the z-direction for various substrate thicknesses. As the substrate thickness decreases, the micropillar stiffness increases. Furthermore, the micropillar sheet with thicker substrate had lateral collapsed at higher compressive load. Unlike micropillar sheets with substrates, the micropillar sheet without the substrate did not experience lateral collapse under the compressive load.

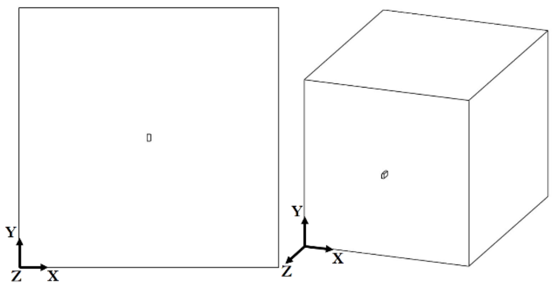

(a)

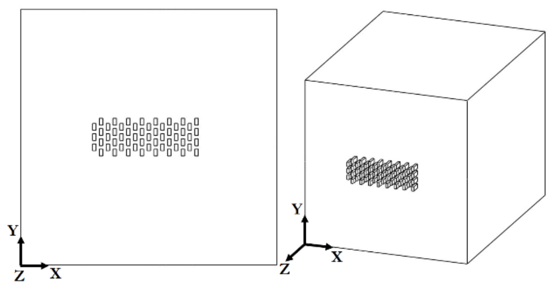

(b)

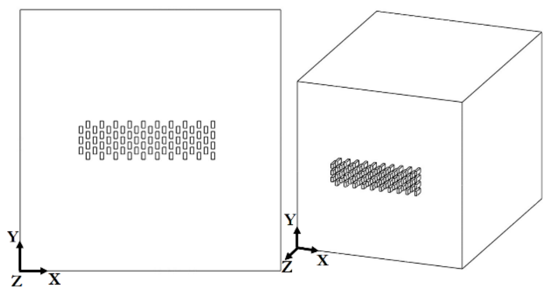

(c)

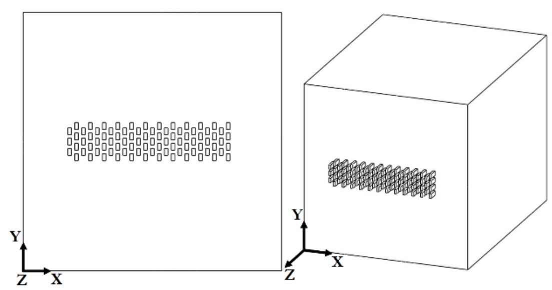

(d)

Fig. 5. FE models of micropillar sheets with the substrate thickness of 1,910 μm for (a) one micropillar, (b) 56 micropillars, (c) 70 micropillars and (d) 84 micropillars.

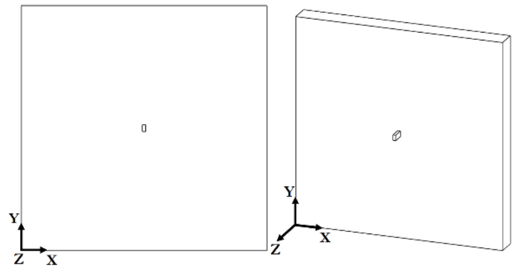

(a)

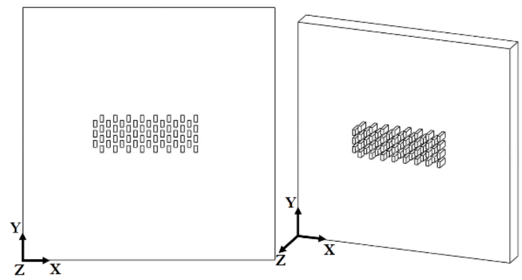

(b)

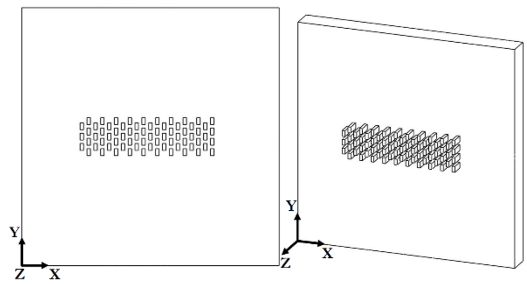

(c)

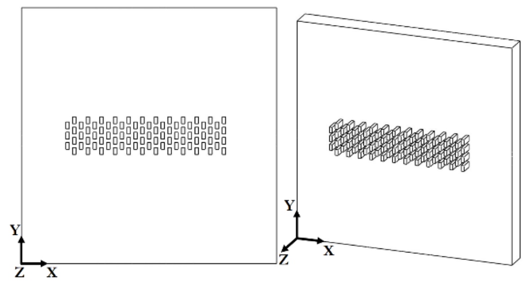

(d)

Fig. 6. FE models of micropillar sheets with the substrate thickness of 150 μm for (a) one micropillar, (b) 56 micropillars, (c) 70 micropillars and (d) 84 micropillars.

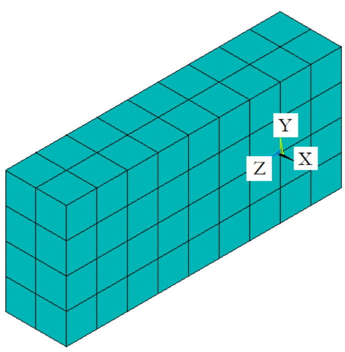

Fig. 7. FE model of a micropillar without a substrate.

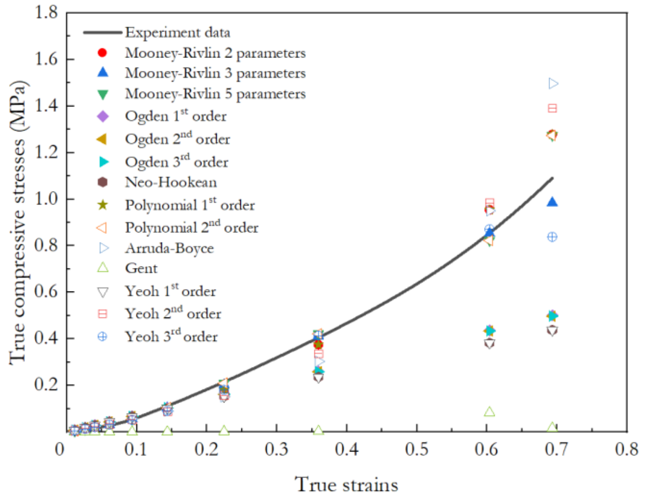

Fig. 8. Plot of true compressive stresses and strains of each FE result of hyperelastic material models compared to experiment data.

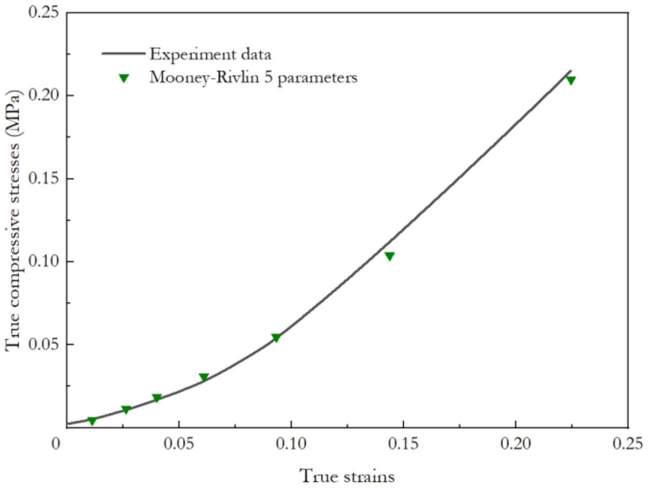

Fig. 9. Plot of true compressive stresses and strains of FE result of Mooney-Rivlin 5 parameters material model compared to experiment data.

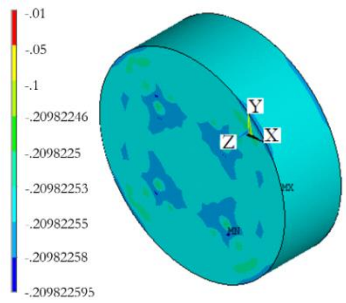

(a)

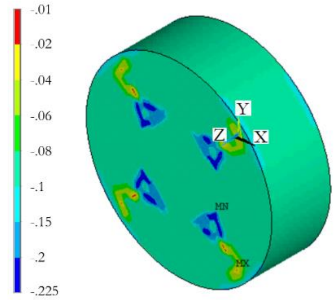

(b)

Fig. 10. Contour plot of (a) stress in z-direction (MPa) and (b) strain in z-direction.

Table 11. The sum square of error of FE results for various hyperelastic material models based on low strain range $(\varepsilon_z \leq 0.225)$.

Hyperelastic material models	Sum square of error (SSE)
Mooney-Rivlin 2 parameters	$1,506.16 \times 10^{-6}$
Mooney-Rivlin 3 parameters	243.45×10^{-6}
Mooney-Rivlin 5 parameters	106.17×10^{-6}
Polynomial 1st order	$1,506.16 \times 10^{-6}$
Polynomial 2nd order	106.39×10^{-6}
Yeoh 1st order	$4,597.73 \times 10^{-6}$
Yeoh 2nd order	$3,925.70 \times 10^{-6}$
Yeoh 3rd order	$1,688.28 \times 10^{-6}$
Ogden 1st order	$3,497.30 \times 10^{-6}$
Ogden 2nd order	$3,538.62 \times 10^{-6}$
Ogden 3rd order	$3,529.11 \times 10^{-6}$
Neo-Hookean	$4,597.73 \times 10^{-6}$
Arruda-Boyce	$4,634.15 \times 10^{-6}$
Gent	$61,978.64 \times 10^{-6}$

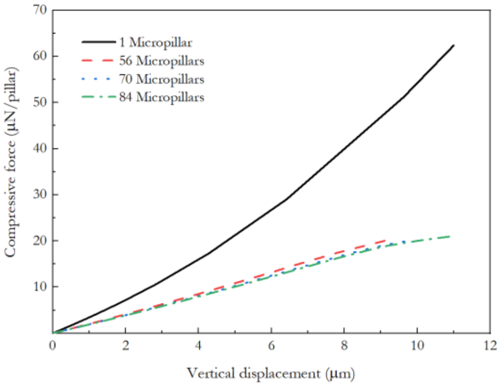

Fig. 11. Plot of compressive force per one micropillar and vertical displacement for 1,910 μm thick substrate.

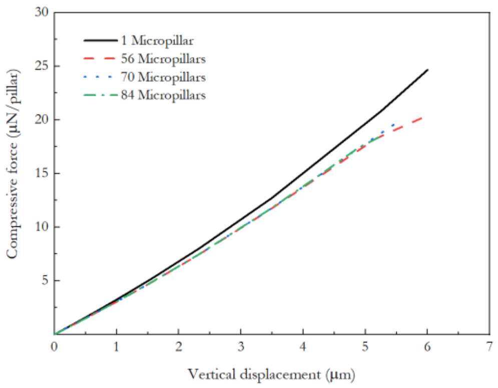

Fig. 12. Plot of compressive force per one micropillar and vertical displacement for 150 μm thick substrate.

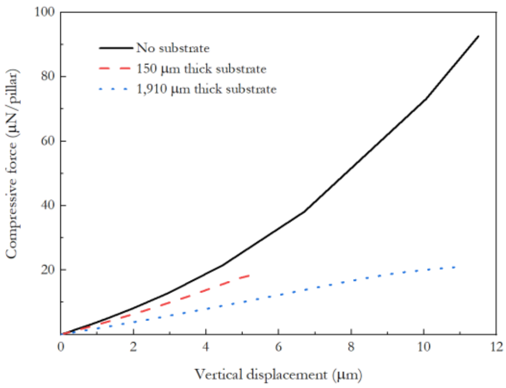

Fig. 13. Plot of compressive force and vertical displacement for various substrate thicknesses.

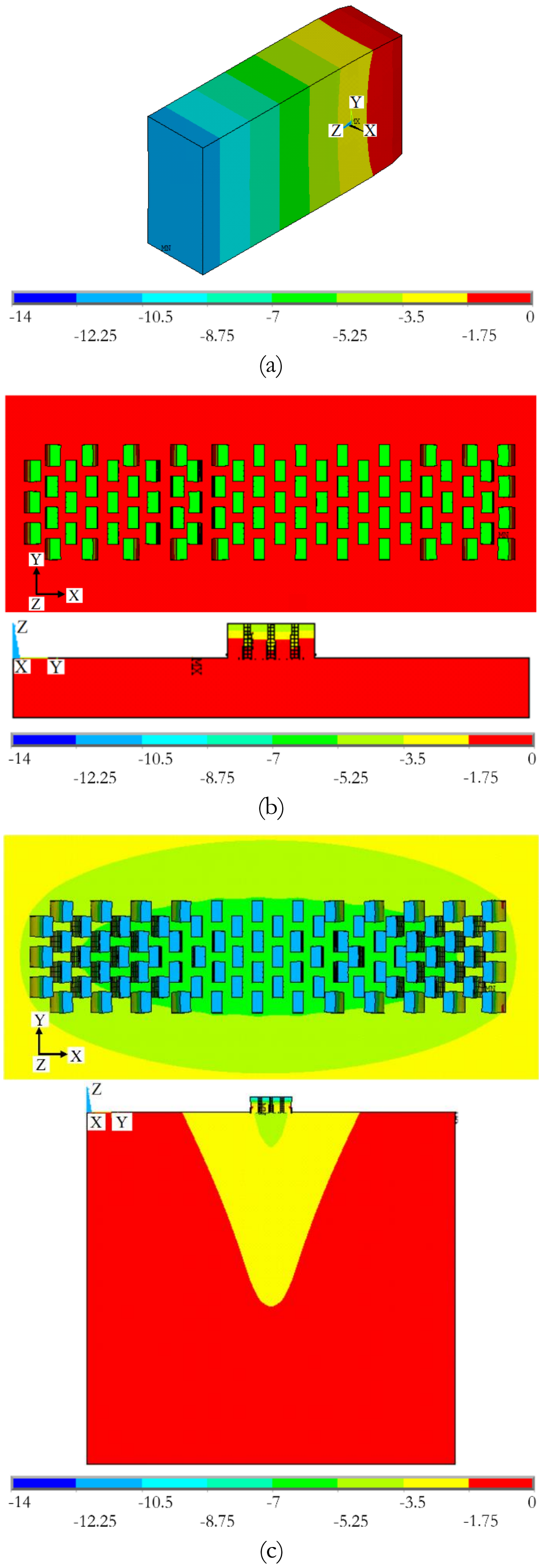

Fig. 14. Contour plot of deformation in the z-direction (μm) at the maximum compressive force for (a) no substrate, (b) 150 μm thick substrate and (c) 1,910 μm thick substrate.

5. Conclusions

The FE model of PDMS compressive specimens equipped with Mooney-Rivlin 5 parameters obtained the most accurate FE results on low strain range of $\varepsilon_{\xi} \leq 0.225$ with SSE of 106.17×10^{-6}. We found the convergence of FE solutions of micropillar sheet models under compressive loading which were 84 micropillars on the substrate. The compressive strength of a micropillar sheet decreases as the thickness of a substrate decreases. The lateral collapses were found on the micropillar sheet and results in loss of its hydrophobic properties. This lateral collapse resulted from non-uniform vertical deformation of the soft substrate under micropillars as illustrated in Fig. 14c. The maximum compressive forces per one micropillar were 21.060 μN for the 1,910 μm thick substrate and 18.549 μN for the 150 μm thick substrate.. Nonetheless, the stiffness of a micropillar sheet significantly increased as the substrate thickness decreased. Unlike micropillar sheets, micropillars without the substrate did not experience lateral collapse. Finally, we also found that substrate thickness effected on the collapse pattern of micropillars in which the collapse initially started from edge to inside of the compressed area.

Acknowledgement

This research was supported by Thailand Graduate Institute of Science and Technology, National Science and Technology Development Agency [contract number SCA-CO-2561-7124TH] and National Electronics and Computer Technology Center (NECTEC), Thailand [FleXARs project, grant number P1951452]. The authors acknowledge all staffs at Thai Microelectronics Center (TMEC), for Si mold fabrication and characterization.

References

[1] G. D. Bixler, and B. Bhushan, "Biofouling: lessons from nature," *Phil. Trans. R. Soc. A*, vol. 370, pp. 2381-2417, May 2012.

[2] A. Sabbah, A. Youssef, and P. Damman, "Superhydrophobic surfaces created by elastic instability of PDMS," *Appl. Sci* vol. 6, pp. 152-159, May 2016.

[3] N. Gao, and Y. Yan, "Modeling superhydrophobic contact angles and wetting transition," *Journal of Bionic Engineering*, vol. 6, no. 4, pp. 335-340, Dec. 2009.

[4] A. M. A. Mohamed, A. M. Abdullah, and N. A. Younan, "Corrosion behavior of superhydrophobic surfaces: A review," *Arabian Journal of Chemistry*, vol. 8, no. 6, pp. 749-765, Nov. 2015.

[5] N. Atthi, O. Nimittrakoolchai, S. Supothina, J. Supadech, W. Jeamsaksiri, A. Pankiew, C. Hruanun, and A. Poyai, "An effect of silicon micro-/nano-patterning arrays on superhydrophobic surface," *J. Nanosci. Nonatechnol*, vol. 11, no. 10, pp. 8967-8973, Oct. 2011.

[6] M. V. Graham and N. C. Cady, "Nano and microscale topographies for the prevention of bacterial surface fouling," *Coatings*, vol. 4, pp. 37-59, Jan. 2014.

[7] Q. Cheng, Z. Sun, G. A. Meininger, and M. Almasri, "Mechanical study of micromachined polydimethylsiloxane elastic microposts," *American Institute of Physics*, vol. 81, Oct. 2010.

[8] D. R. P. Singh, N. Chawla, G. Tang, and Y. L. Shen, "Micropillar compression of Al/SiC nanolaminates," *Acta Materialia*, vol. 58, pp. 6628-6636, Dec. 2010.

[9] K. Thanakhun and T. Puttapitukporn, "PDMS material models for anti-fouling surfaces using finite element method," *Eng. J.*, vol. 23, no. 6, pp. 381-398, Nov. 2019.

[10] S. Johari and L. Y. Shyan, "Stress-strain relationship of PDMS micropillar for force measurement application," in *InCAPE*, 2017, vol. 162, p. 01080, doi: 10.1051/epjconf/201716201080.

[11] M. L. Rathod, N. Pareek, S. Agrawal, S. Jaddivada, D. W. Lee, and N. Gundiah, "Engineered ridge and micropillar array detectors to quantify the directional migration of fibroblasts," *RSC Advances*, vol. 7, no. 18, pp. 51436-51443, Oct. 2017.

[12] T. K. Kim, J. K. Kim, and O. C. Jeong, "Measurement of nonlinear mechanical properties of PDMS elastomer," *Microelectronic Engineering*, vol. 88, pp. 1982-1985, Aug. 2011.

[13] V. Carlescu, G. Prisacaru, and D. N. Olaru, "FEM simulation on uniaxial tension of hyperelastic elastomers," *Applied Mechanics and Materials.*, vol. 659, no. 1, pp. 57-62, May 2014.

[14] J. Phromjan and C. Suvanjumrat, "A suitable constitutive model for solid tire analysis under quasi-static loads using finite element method," *Eng. J.*, vol. 22, no. 2, pp. 141-155, Mar. 2018.

[15] R. Rugsaj and C. Suvanjumrat, "Finite element analysis of hyperelastic material model for non-pneumatic tire," *Key Engineering Materials*, vol. 775, pp. 554-559, Aug. 2018.

[16] D. Cheng, S. S. Sridharamurthy, J. T. Hunter, J. S. Park, N. L. Abbott, and H. Jiang, "A sensing device using liquid crystal in a micropillar array supporting structure," *Journal of Microelectromechanical Systems*, vol. 18, no. 5, pp. 973-982, Oct. 2009.

[17] D. Huri and T. Mankovits, "Comparison of the material models in rubber finite element analysis," *IOP Conf Series: Materials Science and Engineering*, vol. 393, no. 15, 2018.

[18] Y. F. Wu, H. Wang, A. Q. Li, D. M. Feng, B. Sha, and Y. P.Zhang, "Explicit finite element analysis and experimental verification of a sliding lead rubber bearing," *J. Zhejiang Univ-Sci A (Appl. Phys. & Eng.)*, vol. 18, no. 5, pp. 363-376, May 2017.

[19] M. Shahzad, A. Kamran, M. Z. Siddiqui, and M. Farhan, "Mechanical characterization and FE

modelling of a hyperelastic material," *Mat. Res.*, vol. 18, no. 5, pp. 918-924, Jul. 2015.
[20] M. J. G. Ruiz and L. Y. S. Gonzalez, "Comparison of hyperelastic material models in the analysis of fabrics," *International Journal of Clothing Science and Technology*, vol. 18, no 5, pp. 314-325, 2006.
[21] 365 DataScience. "Sum of squares total, sum of squares regression and sum of squares error." http://www.365datascience.com/sum-squares/ (accessed Sept. 4, 2019).
[22] W. Bae, M. K. Kwak, H. E. Jeong, C. Pang, H. Jeong and K. Suh, "Fabrication and analysis of enforced dry adhesives with core–shell micropillars," *Soft Matter.*, vol. 9, no.20, pp. 1422-1427, Nov. 2012.

Thitikan Pakawan received the B.Eng. degree in mechanical engineering from Kasetsart University Sriracha Campus in 2016 and she is currently receiving scholarship from Thailand Graduate Institute of Science and Technology (TGIST), National Science and Technology Development Agency (NSTDA).

Tumrong Puttapitukporn received the B.Eng. degree in mechanical engineering from Kasetsart University, Thailand in 1998, and the M.S. and Ph.D. degree in mechanical engineering from Oregon State University, USA in 1999 and 2003 respectively.

He is currently the Associate Professor in Department of Mechanical Engineering, Kasetsart University, Thailand. His research focus on finite element modeling and applications of generalized continuum theories.

Nithi Atthi received his M.Eng. and Ph.D. in electronics and applied physics from Tokyo Institute of Technology, Japan in 2013 and 2016, respectively.

He has co-authored of 25 technical journal publications, presented his research in 100 conferences and also filed 20 patents. In 2018, he took a position as a research team leader of Surface and Microfluidic Device Innovation Research Team, Thai Microelectronics Center (TMEC), Thailand. His work interest include Si-based semiconductor process technology, micro/nano patterning, high-k/metal gate stacks, microfluidic devices, and superoleophobic surface by surface texturing and modification for various applications

Witsaroot Sripumkhai received M.S. degree in science and nanotechnology from College of Nanotechnology, KMITL, Thailand.

He is currently a Senior Assistant Researcher in Surface and Microfluidic Device Innovation Research Team at Thai Microelectronics Center (TMEC), NECTEC, NSTDA. His research interests Microfabrication process for microfluidic applications and superhydrophobic surface for antifouling application.

Pattaraluck Pattamang received M.S. degree in science and nanotechnology from College of Nanotechnology, KMITL, Thailand.

She is currently an Assistant Researcher in Surface and Microfluidic Device Innovation Research Team at Thai Microelectronics Center (TMEC), NECTEC, NSTDA. Her interests are Microfluidic device and Lab on a disk.

DOI:10.4186/ej.2020.24.4.73

Nipapan Klunngien received the B.Eng. degree in electronic engineering from King Mongkut's Institute of Technology Ladkrabang in 1996 and the M.Sc. and Ph.D. degree in microelectronics from University of Newcastle upon Tyne, Newcastle, UK, in 2005.

Since 2005, she is a researcher at Thai Microelectronics Center (TMEC), National Electronics and Computer Technology Center (NECTEC), Thailand. Her research interests are CMOS technology, semiconductor devices, high-k gate dielectrics, and sensor technology.

Wutthinan Jeamsaksiri received his M.Eng. and Ph.D. from department of electrical and electronic engineering, Imperial College, London in 1996 and 2003, respectively.

He then worked as a process integration engineer on a European project at IMEC, Leuven, Belgium from 2000 to 2004. The project he carried out was on Integration of Microwave Performance Advanced CMOS Technology. From 2005 he has been working at Thai Microelectronics Center (TMEC) under the National Electronics and Computer Technology Center (NECTEC). In 2018 he took the position as a research group director of TMEC. His work interest includes Si based sensors, MEMS, microfluidic devices, and Surface texturing and modification for various applications.